



Cite this: DOI: 10.1039/d0sm02154g

Grafting density induced reentrant disorder–order–disorder transition in planar di-block copolymer brushes

 Barbara Capone,^a Christos N. Likos^b and Ivan Coluzza^c

By means of multiscale molecular simulation, we show that solvophilic–solvophobic AB diblock copolymer brushes in the semi-dilute regime present a re-entrant disorder/order/disorder transition. The latter is fully controllable through two parameters: the grafting density and the solvophobic to solvophilic ratio of the tethered macromolecules. Upon increasing density, chains first aggregate into patches, then further order into a crystalline phase and finally melt into a disordered phase. We demonstrate that the order/disorder transition can be explained through the peculiar properties of the aggregates: upon increasing density, the aggregation number grows as expected. On the contrary, their projection on the plane shrinks, thus melting the emergent ordered phase. Such a density dependent shrinkage, seen for the first time as the cause to an order/disorder phase transition, is as a consequence of the entropic/enthalpic competition that characterises the hierarchical self-assembly of the brush.

 Received 5th December 2020,
 Accepted 4th March 2021

DOI: 10.1039/d0sm02154g

rsc.li/soft-matter-journal

1 Introduction

Polymer brushes are a class of polymeric systems made of macromolecules grafted on one end to a substrate or an interface.¹ The geometry of the grafting substrate and the nature of the grafted macromolecules give rise to a plethora of possible self-organising scenarios.^{2,3} Simple homopolymeric brushes (*i.e.*, brushes made by homopolymers tethered to a substrate) and their properties have been extensively investigated both theoretically^{4–10} and experimentally,^{11–14} corroborating the validity of scaling theories that predicted the dependence of brush height on both grafting density and solvent quality.^{2,3} A considerably more complex scenario results by altering the local chemical composition of the tethered macromolecules. For example, by grafting AB solvophilic/solvophobic diblock copolymers onto substrates of various geometries, it is possible to exploit the rich morphology presented by such macromolecules in solution, to obtain complex coating patterns^{13,15–19} arising from the competition between the entropic steric repulsion among the solvophilic regions of the grafted chains, and the effective enthalpic attraction in solvophobic regions. AB solvophilic/solvophobic diblock copolymer brushes are a particular class of grafted macromolecular assembly, known

to present a very complex self-aggregating scenario^{13,16–19} arising from the competition between the entropic steric repulsion among the grafted chains, and the effective enthalpic attraction in solvophobic regions. Applications of diblock copolymer brushes range from template surface for mesoporous materials,²⁰ to patterned surfaces,¹⁶ and to tissue engineering.²¹ The versatility of diblock copolymer brushes attracted for almost three decades the attention of scientists from diverse sectors.¹⁵ Nevertheless, the prediction of their assembly behaviour still presents a challenging problem. Self-consistent field theory has offered a very powerful tool for the prediction of the behaviour of such brushes for grafting densities starting from the melt, down to the semi-dilute regime.^{16,22–24} Here, fluctuations in density weaken the predictive power of mean-field based approaches, rendering computational methods as the main but not always exhaustive exploration tool due to the large number of parameter involved.

In this paper, we focus on the self-assembly properties of neutral AB diblock copolymer brushes, made of A-solvophilic heads grafted on an entropically repulsive planar surface, and of B-solvophobic ends exposed to the solvent, in the semi-dilute regime. Furthermore we will assume that the number of A monomers $L_A \gg 1$ and the number of B monomers $L_B \gg 1$. Starting from a dilute system we establish, upon increasing grafting density, the emergence of patches on the surface, the ordering of such patches into a crystalline phase and in particular an unexpected re-entrant order–disorder phase transition.

The equilibrium phase diagram of diblock copolymer brushes generically depends on two parameters that balance the weight of the entropy/enthalpy contributions. The first is the fraction α of

^a Science Department, University of Roma Tre, Via della Vasca Navale 84, 00146, Rome, Italy. E-mail: barbara.capone@uniroma3.it

^b Faculty of Physics, University of Vienna, Boltzmanngasse 5, A-1090 Vienna, Austria

^c Center for Cooperative Research in Biomaterials (CIC biomaGUNE),

Basque Research and Technology Alliance (BRTA), Paseo de Miramon 182, 20014, Donostia San Sebastián, Spain

solvophobic monomers per grafted chain, while the second is the ratio σ/σ^* between the surface grafting density σ and the overlap value $\sigma^* = (\pi R_g^2)^{-1}$ of the same, *i.e.*, the density at which two neighbouring grafted chains of length L and radius of gyration $R_g \sim L^\nu$ would on average overlap. The resulting $(\sigma/\sigma^*, \alpha)$ -phase diagram can be broadly divided in: an entropy-dominated region, where the steric repulsions between the grafted chains dictate the global behaviour of the system, and an enthalpy dominated one where the solvophobic ends start to interact.^{16,24} The entropy dominated phase of the $(\sigma/\sigma^*, \alpha)$ -phase diagram, is a region in which – on average – the terminal ends of the grafted diblocks do not interact. The grafted polymeric chains fluctuate similarly to homopolymeric chains and no significant aggregation is seen on the grafted substrate. As the $(\sigma/\sigma^*, \alpha)$ combination allows for a non zero probability of binding of the terminal solvophobic ends, we enter, upon increasing σ/σ^* or α , the enthalpy-dominated region. Here, the density of attractive monomers in solution is sufficiently high, and the latter aggregate and form clusters (patches), that then fluctuate on a “soft substrate” of solvophilic heads.

The rest of the paper is organised as follows: we first describe the system, then introduce an in depth description of the coarse graining strategy employed to represent the polymeric macromolecules, simulation methods and the main results on the phase diagram. Conclusions are followed by an Appendix section where all technical details and data for all of the analysed systems are discussed in depth.

2 Methods

The transition from the entropy to the enthalpy dominated phase is where the self-assembly process takes place, and it lies in the semi-dilute regime. The exploration of such a density region is challenging computationally, as all equilibrium properties are strongly affected by spatial inhomogeneity, local density fluctuations, and finite size effects,²⁵ thus requiring the analysis of extremely large systems. To this end we make use of the Soft-Effective-Segment (SES) coarse-graining methodology,^{26,27} an approach that allows to explore large systems, made of thousands of chains each consisting – in its full monomer representation – of thousands of monomers. SES has been already proven to be able to quantitatively characterise equilibrium properties of macromolecular assemblies of the most diversified geometrical and chemical composition, with continuous possibility of backtracking the coarse grained results onto a well defined underlying monomer described system.^{27–30}

The original, microscopic lattice model of each grafted polymer is thus mapped onto a coarse-grained SES description,^{27,28,31,32} based on renormalized chains of weakly interacting mesoscopic segments. Within such a representation, groups of monomers are represented by means of first principles effective potentials, retaining all information on temperature, solvent quality and many body contributions.^{26,27,33} The gain of this coarse-grained description is the considerable reduction of the number of degrees of freedom, for $3L$ to $3n$ per polymer (where L is the number of monomers per chain, while n is the number of beads – or

blobs – used to represent the chain in a coarse grained way), as well as the soft nature of the effective interactions allowing large scale simulations of systems involving many, high molecular weight ($L \gg 1$) polymers in the semi-dilute regime. Each blob represents a subpart of the polymeric chain containing a number L/n of monomers, and radius of gyration $r_g \sim (L/n)^\nu$, where ν is the original Flory exponent of the chain that is being coarse-grained. The number n of blobs used to represent each coarse-grained polymeric chain, depends on the solution density N/V , where N is the number of polymers, and V the volume occupied by the solution. n is chosen so that the local blob concentration $\rho_{\text{blob}} = nN/V$ is below the blob overlap density $\rho_{\text{blob}}^* = 4/3\pi r_g^3$. Therefore we will always use, for all of the analysed grafting densities, a number of blobs so that $\rho_{\text{blob}} < \rho_{\text{blob}}^*$. It is important to notice that this coarse-graining procedure holds valid till the number of Kuhn segments (monomers) per blob is high enough to retain polymer scaling properties: $L/n \sim 30$. Under those conditions, the SES coarse-graining method has already been proven to match quantitatively microscopically described systems^{27,28,31,32,34} Capone *et al.* have extended the SES representation from homopolymers to di-block polymers²⁸ for single chains and telechelic star polymers.³⁵

2.1 The effective potentials

To represent the system in a coarse-grained way, polymer chains of length L are divided into n segments – or blobs, each one made of a number L/n of monomers. Blobs are interacting with one each other through effective interactions; the interactions between blobs are determined by a first principles inversion procedure, that was derived for diblock copolymers,^{27,28} generalising the method used earlier for the simple dumbbell representation of the same.^{31,36,37} The three intramolecular tethering potentials, consisting of a superposition of repulsive and attractive terms, are determined from microscopic, full-monomer Monte Carlo simulations of an isolated α - β di-block copolymer, $\alpha, \beta = A, B$, where the A-block is in good solvent and the B-block is just below the θ solvent. The distribution function $s_{\alpha\beta}(r)$ of the separations between the centers of mass of the two blocks is estimated by averaging over a large number of monomer-configurations, and the corresponding tethering potential follows from:

$$\varphi_{\alpha\beta}(r) = -k_B T \ln[s_{\alpha\beta}(r)]. \quad (1)$$

In order to determine the intermolecular pair potentials, we consider the six possible combinations of $\alpha\beta$ and $\gamma\delta$ dimers and calculate the corresponding blob–blob pair correlation functions $h_{\alpha\gamma}(r)$, as functions of the distance r between the centres of masses of the α -block of dimer 1 and the γ -block of dimer 2. This is achieved from Monte Carlo-generated histograms, by averaging over allowed monomer configurations for fixed values of r , according to the usual Metropolis algorithm. The functions $h_{\alpha\gamma}(r)$ are mapped out by varying the distance r , *i.e.*, by gradually moving the CM's towards each other. The effective pair potentials are extracted by inverting the pair correlation functions according to an exact cluster expansion, valid for an

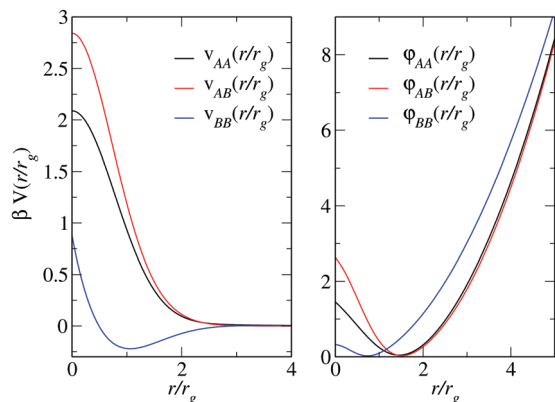


Fig. 1 The non-bonded potentials V_{AA} in black, V_{AB} in red and V_{BB} in blue and the tethering potentials ϕ_{AA} in black, ϕ_{AB} in red and ϕ_{BB} in blue between the centers of mass of the various blobs of type A and B. The radius of gyration of the A and B blobs is the same and labelled as r_g .

isolated pair of dimers, *i.e.*, in the low density limit.^{27,28,31,36–38} The effective intermolecular potentials $V_{\alpha\beta}(r)$ and the intramolecular tethering potentials $\phi_{\alpha\beta}(r)$ obtained by the inversion

procedure are shown in Fig. 1, as functions of the CM–CM distance r , reduced by the common blob radius of gyration r_g . The molecular weights of the polymer segments comprising each blob, used in the simulations, are sufficiently large ($m_A, m_B \geq 100$) to justify the statement that the data shown in Fig. 1 indeed correspond to the scaling limit.

2.2 Simulation methods

The simulation consists in random translations of the single segments that are accepted or rejected according to the Metropolis rule.³⁹ Since the system undergoes disorder–order transitions we have included a box reshaping move where the aspect ratio of the grafting ratio is slowly changed. The deformation is accepted or rejected according to the Metropolis rule.

We here consider brushes made of diblock copolymer chains of length $L = 10^6$ monomers, with a percentage α of solvophobic monomers spanning the range from 40% up to 80%. We investigate a wide range of grafting ratios σ/σ^* from 1 up to 26. It is important to stress that the range is within the semi-dilute regime and we do not reach the melt where we expect a lamellar phase with a solvophobic layer standing on a

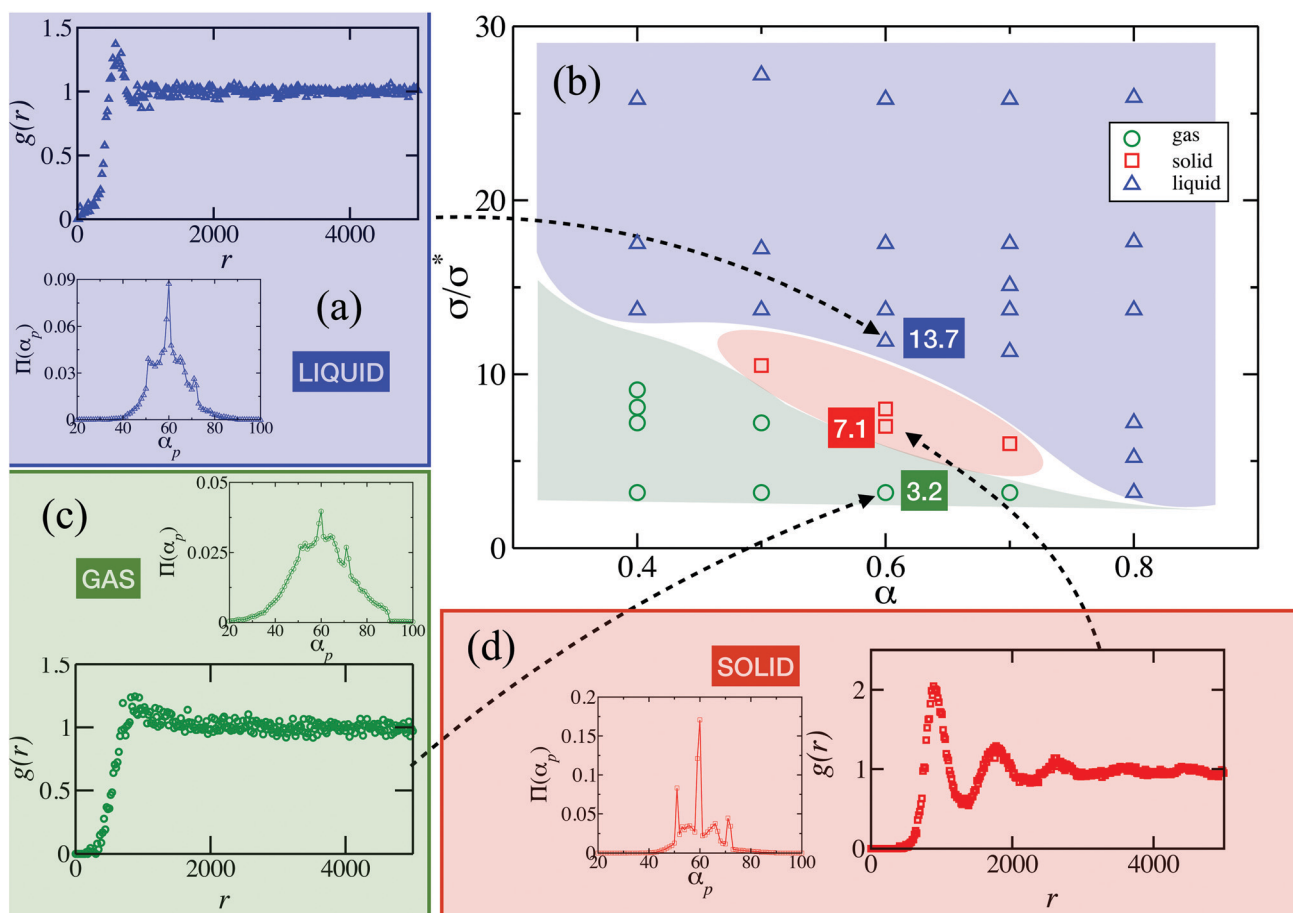


Fig. 2 Phase diagram for the gas–solid–liquid transition as a function of the asymmetry ratio α and the density ratio σ/σ^* in panel (b). It is possible to see the appearance of the solid phase as a re-entrant phase (in red – panel (d)) squeezed between the gas (green – panel (c)) and liquid (blue – panel (a)) phases. In the panels we follow the transition along the $\alpha = 0.6$ line. In every panel we show the distribution $\Pi(\alpha_p)$ of the angle α_p between pairs of first neighbouring patches (see Section A.2), and the radial distribution $g(r)$ of the solvophobic monomers, where r is the distance between the centres of masses of the aggregates expressed in units of the persistence length b of the underlying microscopic representation.

solvophilic one. In the semi-dilute regime, the SES coarse graining procedure has been shown to be able to quantitatively reproduce properties of the corresponding microscopic system.^{27,28,31,32,34} All results presented in this work are in scaling, and they thus only are functions of α and σ/σ^* . Diblock copolymer brushes made of polymers of a different length (in scaling), would therefore reproduce the same behaviour here presented, provided that α and σ/σ^* are kept constant. All distances are reported in units of the bond length b of the underlying full monomer representation, while free energies (effective interactions between beads) are in units of $k_B T$; temperatures are expressed in reduced units, where room temperature corresponds to $T = 1$. To speedup equilibration and sampling, we employ the Virtual Move Parallel Tempering (VMPT)⁴⁰ method, which in our previous studies on homopolymer brushes, has proven to be extremely effective in sampling the brush profiles.^{9,10} A typical VMPT simulation is performed at different reduced temperatures (4.0, 3.5, 3.0, 2.7, 2.5, 2.2, 2.0, 1.5, 1.2, 1.1, 1.0, 0.8, 0.5, 0.3, 0.2, 0.1), we run the simulation in parallel at higher additional temperatures to help overcome barriers in the phase space. However, we are only interested in the behaviour of the system at the reduced temperature $T = 1$ where the SES potential are valid. We have considered both the scenarios where the anchoring point is fixed or mobile on the grafted surface, without observing a significant difference in the behaviour of the copolymer brush, as previously reported for the case of homopolymeric brushes.^{9,10} The reason is that the chains are long and well above the scaling limit which is imposed by SES representation.

3 Results

By collecting all our simulations, we can sketch a phase diagram for the system as a function of the $(\sigma/\sigma^*, \alpha)$ combination, as drawn in Fig. 2.

The green area in panel (b) of Fig. 2 shows the $(\alpha, \sigma/\sigma^*)$ region where there is no significant inter-molecular interaction between the solvophobic tails of the different macromolecules (gas-phase). The brush remains in an “open” configuration. Such a phase is characterised by a carpet of isolated collapsed tails monomers, each anchored to the surface *via* its solvophilic head (see Fig. 3a). The σ/σ^* boundary of the gas phase shrinks with increasing α indicating that aggregates forms only when the density of attractive monomers is over a minimum value.

When the local monomeric density of the solvophobic terminal ends reaches a threshold, tails belonging to different chains aggregate into functionalised regions, or patches. As the latter are formed, they are expelled from the solvophilic region of the brush and exposed to the solvent. Each aggregate takes the shape of a “pinned micelle”^{16,24} where the core region is formed by the clustered attractive tails, and a corona tethered to the surface is formed by the corresponding self-avoiding heads (see Fig. 3c). The patches fluctuate, on average, around an equilibrium planar configuration parallel to the grafted substrate.

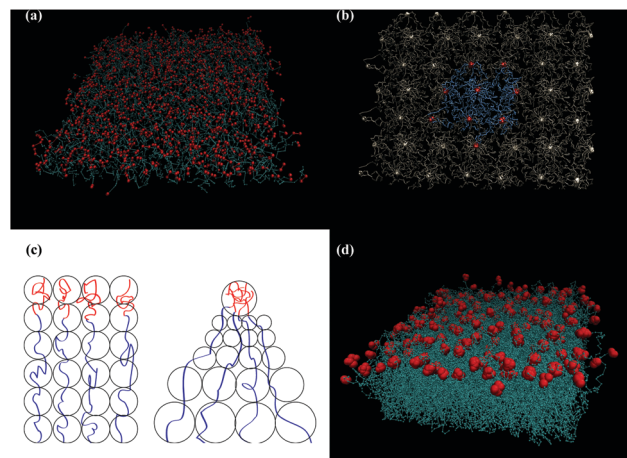


Fig. 3 Snapshots of the typical diblock copolymer brush conformations for the three different phases (a) gas, (b) solid (d) liquid. (c) Left: Sketch of the chains at the end of the brush: the end of the chains are not cross-interacting and cover uniformly the surface of the brush. (c) Right: Sketch of the pinned micelles in the aggregated phases (solid and liquid). (d) snapshot of the re-entrant liquid. Upon increasing the ratio σ/σ^* the aggregates melt the 2D-crystalline pattern shown in (b). In all snapshots, red are the solvophobic monomers, cyan are the solvophilic ones.

The region $\alpha \in [0.5, 0.7]$ shows for $\sigma/\sigma^* \in [7.0, 13.0]$ (red squares in Fig. 2b) the emergence of an ordered 2D crystalline phase, or solid-phase (see Fig. 3b). This phase is suppressed when the grafting density is further increased: patches lose their 2D order and fluctuate in both parallel and orthogonal directions on a plane parallel to the grafting surface, and a liquid-phase arises from the crystalline region (see Fig. 3d). It is important to stress that for $\alpha = 0.4$ the system goes directly from the gas- to the liquid-phase, while for $\alpha = 0.8$ we only observe the liquid-phase.

For clarity reasons, we here focus on the description of the re-entrant transition for the $\alpha = 0.6$ system; however the phenomenology is valid for all the all of the asymmetry ratios we analysed $\alpha \in [0.4, 0.8]$ and all grafting densities, as we report in detail in Section A. The self-assembly behaviour involves the collapse of multiple chains into the pinned micelle configuration. We hence employed a cluster analysis algorithm (see description in Section A.2) to characterise size, height distribution $\phi(z)$ of the patches with respect to the grafting surface, and the relative arrangement of the aggregates through their pair distribution function $g(r)$ and the distribution $\Pi(\alpha_p)$ of the α_p angles between neighbouring patches (see definitions in Section A.2, and graphical representation in Fig. 9).

The cluster analysis in the gas-phase indicates the coexistence of small intermolecular and many intramolecular clusters (see the black histogram in Fig. 4). In this case, the $g(r)$ between patches does not present any sign of structure and the angular distribution $\Pi(\alpha_p)$ between neighbouring patches is featureless (see green inset in Fig. 2 and in the $g(r)$ s reported in Fig. 10 and 13, pertaining to the “gas” phase).

In the solid-phase, all grafted chains participate to the formation of patches of finite size, that align along preferential directions with respect to the grafting plane. A strong signature

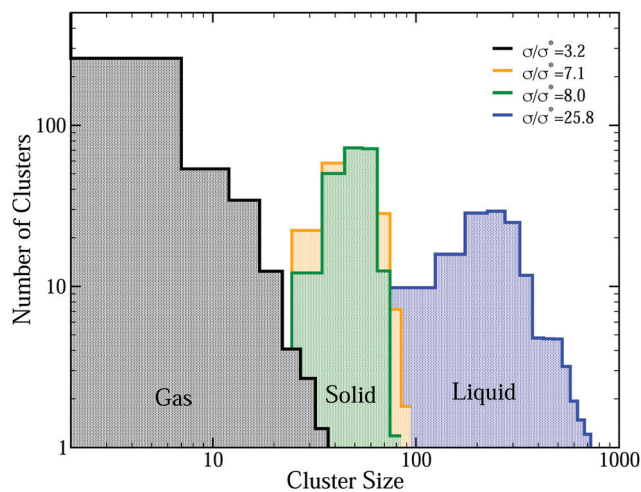


Fig. 4 log–log plot of the number of clusters as function of their size for the gas, solid, and liquid phases for the $\alpha = 0.6$ system. The corona radius of gyration R_{corona} of the clusters in three phases are respectively: 1207, 762 and 483 in units of bond length. To stress the dependence of the phase on the cluster size, we show two different values of σ/σ^* ($\sigma/\sigma^* = 7.1, 8.0$), characterised by a very similar average number of clusters, and both belonging to the solid phase.

of structure is seen in both the radial distribution function between aggregates, and the average angle distribution between neighbouring patches, that sharply distributes around 60° as shown in the red inset of Fig. 2 (and in Fig. 14). The size of the unit cell of the assembled crystals is controlled by the radius R_{corona} . The latter is defined as the average radius of the 2D projection on the grafted surface of the pinned micelles' coronas (see Section A.1 for definition and graphical clarification). By normalising the radial distances by R_{corona} , the first peak of the crystalline $g(r)$ re-scales to unity, as shown in the inset of Fig. 11. Furthermore, the disorder–order transition between the gas and solid-phases distributes the patches at a fixed height from the underlying surface, as shown in Fig. 5. As the grafting density is further increased, the patches start oscillating both in the z -direction, as well as in the xy -plane. Order gets lost and we see the appearance of the liquid-phase.

In the blue inset of Fig. 2 (and in Fig. 12) we show the 2D radial distribution function computed on the projection on the xy plane of the coordinates of the centre of mass of the patches, for the high overlapping densities $\sigma/\sigma^* > 13$. The $g(r)$ shows short-range oscillations typical of a fluid phase, where translational order decays rapidly with the intraparticle distance. The angular distribution $\Pi(\alpha_p)$ in the blue inset of Fig. 2 (and in Fig. 15) also shows a strong loss of order: the sharp peak around 60° appears smoothed with respect to the solid one, resembling more and more to the gas-phase one in Fig. 13. We will thus interpret all of the phases characterised by such a combination of $g(r)$ and $\Pi(\alpha_p)$, as liquid-phases.

In Fig. 4 we show the cluster size distribution for the three phases. The gas-phase presents the coexistence of single chain intramolecular clusters with small intermolecular clusters. Aggregates formed in the solid phase are quite monodisperse, with a cluster size distribution that is sharply peaked. As soon

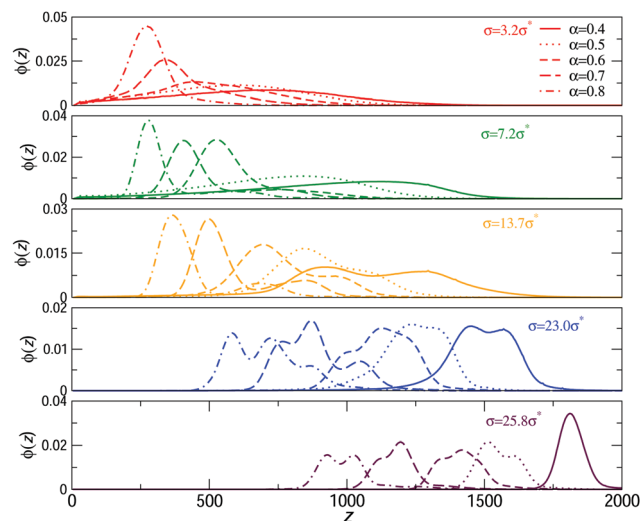


Fig. 5 Height distribution of the solvophobic ends of the brushes with asymmetry ratio $\alpha \in [0.4, 0.8]$ and $\sigma/\sigma^* \in [3.2, 25.8]$. Same colour indicates same grafting density (red $\sigma = 3.2\sigma^*$, orange for $\sigma = 7.2\sigma^*$, green for $\sigma = 13.7\sigma^*$, blue for $\sigma = 23\sigma^*$ and maroon for $\sigma = 25.8\sigma^*$) and same line style indicates same α . The coarse grained approximation used for all the presented analysis is valid for all grafting densities, as the coarse grained system has been represented with a high enough number of blobs to grant that blobs are below their overlap concentration.

as density is increased, and the crystal melts in favour of a liquid-phase. The average cluster size grows, and the width of the cluster distribution spreads. On the other hand, R_{corona} decreases *e.g.*, by $\sim 40\%$ for the $\alpha = 0.6$ case, passing from 762[b] (bond lengths) in the crystal phase ($\sigma/\sigma^* = 7.1$) to 483[b] deep in the liquid phase ($\sigma/\sigma^* = 25.8$). The reduction in the coronae of the pinned micelles can also be appreciated by comparing the solid and liquid $g(r)$ (see Fig. 11 and 12). The position of the first peak – in microscopic units – is centred around 1000[b] for the solid case, while the liquid phase shows an average distance between nearest neighbours of about 500–600[b].

To understand such an apparently counter-intuitive behaviour, we analyse the scaling of the average brush height as a function of density. Reminiscent of the scaling of a homopolymer brush, we observe that, as grafting density is increased, the brush as a whole is stretched, and patches are clearly expelled outwards. Reaching the liquid phase, the aggregates float on a carpet of fully stretched solvophilic chains, see Fig. 16. To formalise the correlation between the stretching of the brush and the shrinkage of the corona radius, we performed a scaling analysis where R_{corona} is obtained by minimizing the total free energy of the pinned micelles for every density (for the detailed derivation of the scaling theory, see Section A.1). Taking into account the free energy contributions of both the packing of the monomers in the patch, and the stretching of the chains belonging to the coronae, scaling theories (see Section A.1) confirm that R_{corona} decreases with as σ/σ^* grows, as shown in Fig. 6. Hence, the re-entrant behaviour is the result of two concurring effects: the reduction of the R_{corona} , and the loss of the 2D confinement manifesting in the double peaks of the height of the tail monomers plotted in

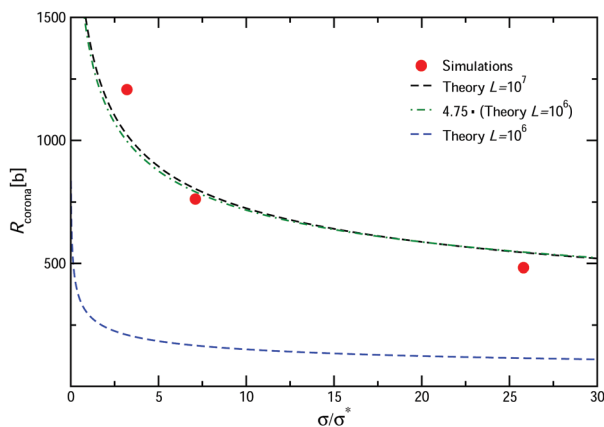


Fig. 6 The quantity R_{corona} obtained by solving (9) for the $\alpha = 0.6$, $L = 10^7$ is plotted as a function of σ . The error bar of the points is smaller than point size. The horizontal axis is in units of σ/σ^* , while the vertical axis is in units of the persistence length $a_B = a_A = b$ of the underlying full monomer representation. The corona radius appears to clearly decrease upon increasing σ . The profile goes through the simulations points (red points) without fitting, however the polymer length L is larger than the one considered in the simulation ($L = 10^6$) because we did not include scaling prefactors in the derivation of R_{corona} . We also show the curve corresponding to the $L = 10^6$ case (blue) and $L = 10^6$ multiplied by a factor 4.75 (green). The latter is practically indistinguishable from the $L = 10^7$ case.

Fig. 5. The latter is reminiscent of the phase observed in core-softened colloids by Osterman *et al.*⁴¹ The arising of the double peak is strongly related to a specific range in grafting densities in the liquid: in such a phase the blobs do not have a planar ordering, and the average height from the grafting substrate fluctuates. On the contrary, in the “solid” phase, the fluctuations along the z axis of the average position of the patches are suppressed.

The free energy analysis is not able to capture the transition between the different phases, as the scaling theory is performed on the single aggregate. It can be therefore only be used to predict how diblock copolymers would arrange within one aggregate (see Section A.1), but it has no predictive power over how different aggregates would distribute with respect to one each other. Nevertheless, the scaling analysis qualitatively reproduces the trend, modulus a constant prefactor that were neglect in the scaling calculation. The qualitative match between the trend of the simulated and calculated R_{corona} is further proof that the SES is capable of reproducing the correct scaling laws of the underlying microscopic system even below the θ temperature.

4 Conclusions

In this work we analysed the properties of solvophilic/solvophobic diblock copolymer brushes in the semi-dilute regime. The computational investigation was made through a coarse grained approach known as the soft-effective-segment methodology,^{28,31} that allows to regroup thousands of monomers into an effective potential, while retaining quantitative predictions on equilibrium properties of the system. We analysed the self-assembling properties

of substrates grafted by thousands of polymers each made of millions of monomers.

We mapped the configurational space of the brush into the phase space of the σ/σ^* , α parameters that fully control the self-assembling properties of brush. We identified the presence of a re-entrant disorder/order/disorder transition in the σ/σ^* , α phase space. The ordered phase corresponds to a 2D crystalline array of patches formed by the assembled solvophobic tails of the polymers. We show how to control the crystalline order by changing the σ/σ^* , α parameters. Hence, producing a tunable crystalline surface with many applications for patterning and templating the growth of materials from the surface. The second key observation that we performed concerns the mechanism for the re-entrant transition. We have demonstrated, both computationally and theoretically, that the increase in the grafting density stretches the pinned micelles outwards reducing their 2D effective radius. To the best of our knowledge such a mechanism has never been observed as a function of grafting density before and represents a novel physical approach to control the ordering of a 2D system. In particular the ordered phase has not been experimentally observed yet. The results presented in Fig. 2 offers a precise map to guide potential new experiments. In the pioneering works by Wang and Müller,⁴² by using a single-chain-in-mean-field (SCMF) simulations approach, the authors observed a related re-entrant transition by varying the asymmetry ratio α ($1 - f$ in their paper). However the underlying mechanism causing the re-entrant transition differs from what presented here, as lateral size of the clusters (patch size) that the authors of ref. 42 find in the re-entrant liquid phase does not decrease when the solid phase melts, but clusters fuse upon forming an almost bi-continuous phase that might be the precursor of the lamellar phase. We did not reach such high grafting densities with our analysis but focused on the semi-dilute regime.

Conflicts of interest

There are no conflicts of interest to declare.

A Appendices

A.1 Scaling theory for the radius of core and corona in pinned micelles

We assume that the surrounding solution is good for the A block, *i.e.* $\theta_A = (T - \Theta_A)/T > 0$ and poor for the B block, *i.e.* $\theta_B = (\Theta_B - T)/T > 0$.

As temperature in the whole work will remain unchanged, θ_A and θ_B are constants that will be neglected in the following part of this derivation. We will deal in this section with scaling theories developed for chains tethered by the soluble A block.

Employing the scaling theories developed in ref. 16, 24 and 43, we write the total free energy F_{TOT} of a pinned micelle as the free energy F_B of the collapsed region (patch), plus the surface free energy F_S between the patch and the corona plus the term F_A as the free energy of a spherical brush.^{16,24} Within the B-block

the free energy of the monomer–monomer interaction is independent of the total number of chains in the micelle and coincides with the free energy in the collapsed core of a single chain (isolated diblock in solution). We can therefore omit it from further consideration because it does not contribute to the free energy difference between chains and spherical micelles.

$$F_{\text{TOT}} = F_B + F_S + F_A. \quad (2)$$

We will analyse separately the three distinct contributions to the total free energy.

The stretching free energy of the B blocks in the core of the micelle can be written as:

$$F_B \sim \frac{R^2}{R_g^2} \sim \frac{R^2}{a_B^2 L_B^{2\nu_B}}, \quad (3)$$

where R is the radius of the patch (of the core of the pinned micelle).

The surface free energy F_S is the free energy associated with the surface between the core and the corona and it is proportional to the ratio between the surface area per chain s defined as

$$s \sim \frac{a_B^3 L_B}{R} = \frac{a_B^3 \alpha L}{R}, \quad (4)$$

and the area occupied by each monomer:

$$F_S \sim \frac{s}{a_B^2} = \frac{a_B^3 \alpha L}{a_B^2 R} = \frac{a_B \alpha L}{R}, \quad (5)$$

where $L_B = \alpha L$.

For long tethered A-parts (height of the brush much larger than the radius R the patch) the system can be viewed as a planar brush covered by spherical micelles, as sketched in Fig. 7.

For this reason, the free energy term F_A that accounts for the contribution of the tails, can be split into two terms: $F_A = F_A^{\text{brush}} + F_A^{\text{micelle}}$, where

$$F_A^{\text{brush}} \sim L_A (\sigma a_A^2)^{1/2\nu_A} = (1 - \alpha)L (\sigma a_A^2)^{1/2\nu_A} \quad (6)$$

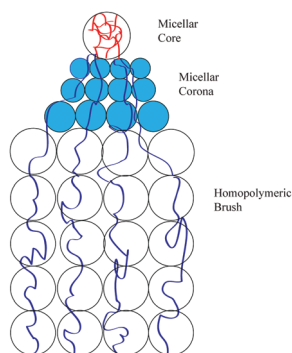


Fig. 7 Pinned micelles are considered as the superposition of a homopolymeric brush plus the fraction of a diblock copolymeric micelle. The red terminal blocks indicate the micellar core assembled by the terminal B blocks, the cyan blobs are the contribution arising from the micellar corona. The white blobs are the homopolymeric brush.

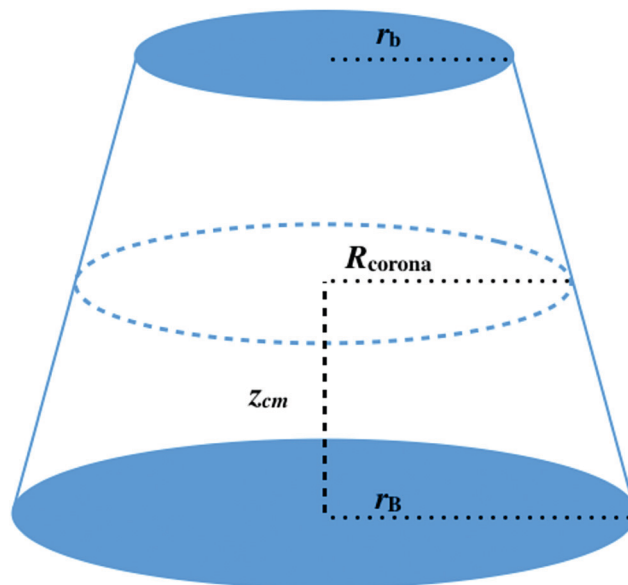


Fig. 8 Sketch of the relation between the corona radius R_{corona} , the patch radius r_b and the radius r_B of the basis of the cone.

and F_A^{micelle} is the free energy of the spherical micelle (see eqn (A1.22)⁴³)

$$F_A^{\text{micelle}} = \frac{\nu_A R}{H_A} F_A^{\text{brush}} \ln \left(1 + \frac{H_A}{\nu_A R} \right) \quad (7)$$

where $L_A = (1 - \alpha)L$ and $H_A = (1 - \alpha)L(\sigma a_A^2)^{(1-\nu_A)/2\nu_A}$. By writing explicitly the total free energy, we obtain:

$$F_{\text{TOT}} = \frac{R^2}{a_B^2 (\alpha L)^{2\nu_B}} + \frac{a_B \alpha L}{R} + F_A^{\text{brush}} + \frac{\nu_A R}{H_A} F_A^{\text{brush}} \ln \left(1 + \frac{H_A}{\nu_A R} \right), \quad (8)$$

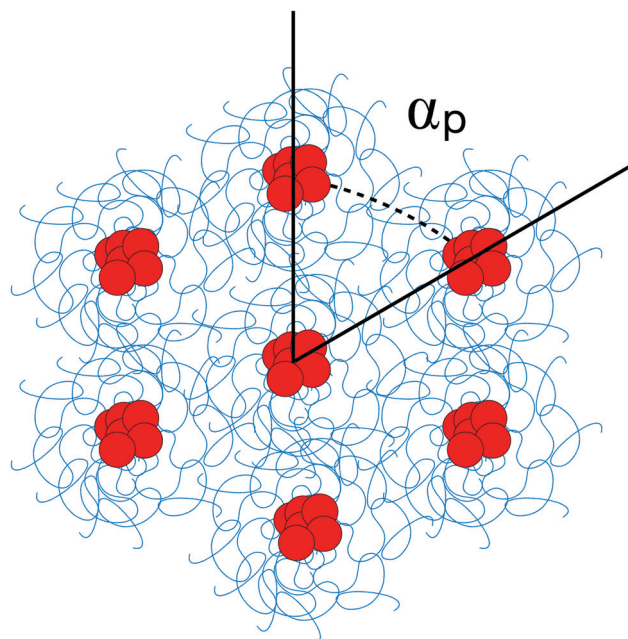


Fig. 9 Schematic representation of α_p , defined as the angle between a cluster and its first neighbour.

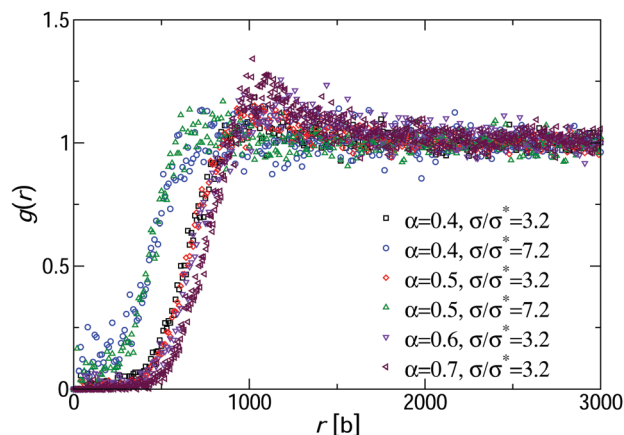


Fig. 10 The radial distribution function between all of the attractive monomers belonging to the grafted diblock copolymers. For the different asymmetries [$\alpha \in 0.4, 0.7$] considered we observed the gas phase at the plotted grafting densities. The x-axis is in units of the bond length.

By minimising the free energy with respect to the radius of the patch R , and remembering that $\partial F_A^{\text{brush}}/\partial R = 0$, we obtain the estimate for the equilibrium patch radius:

$$\frac{\partial F_{\text{TOT}}}{\partial R} = \frac{2R}{a_B^2(\alpha L)^{2\nu_B}} - \frac{a_B \alpha L}{R^2} + \nu_A F_A^{\text{brush}} \times \left[\frac{1}{H_A} \ln \left(1 + \frac{H_A}{\nu_A R} \right) - \frac{1}{(\nu_A R + H_A)} \right] = 0, \quad (9)$$

which we solve for R numerically.

Each pinned micelle is made of f chains tethered on a plane, and the geometry of the aggregate can be approximated as a truncated cone, with radius of the smallest base $r_b = R$ and the radius of the largest base $r_B = (f/\sigma)^{1/2}$ where σ is the grafting density. By assuming that the radius of the patch is made by the close packing of a chain made by f segments of length αL each, we can estimate that

$$R \sim (f\alpha L)^{1/3}, \quad (10)$$

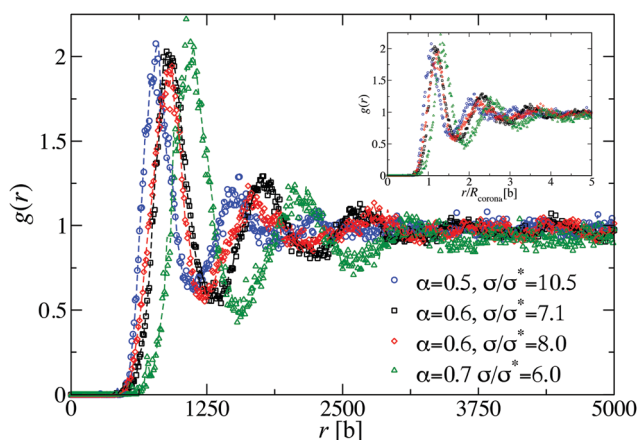


Fig. 11 Pair correlation function between formed patches for different asymmetries [$\alpha \in 0.5, 0.7$] in the region of the configurational space where the solid phase is dominant. In the inset the distances r have been re-scaled by the radius of the corona of the pinned micelles. This re-scaling highlights that patches on average distribute at distances $r = R_{\text{corona}}$.

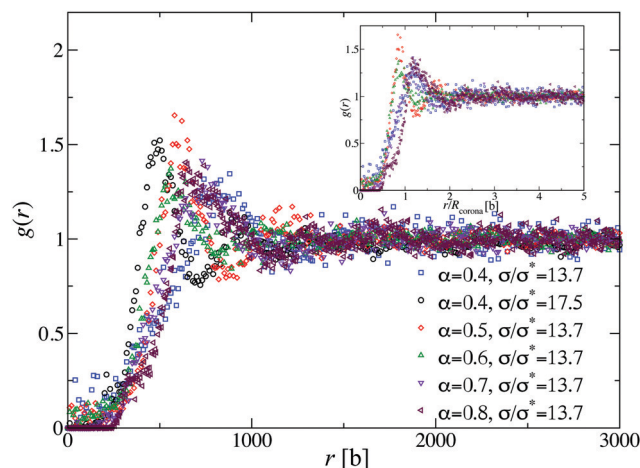


Fig. 12 Pair correlation function between formed patches for different asymmetries [$\alpha \in 0.5, 0.8$]. In the inset the distances r have been re-scaled by the radius of the corona of the pinned micelles. This re-scaling highlights that patches on average distribute at distances slightly below $r = R_{\text{corona}}$. We here see the typical structure of a liquid.

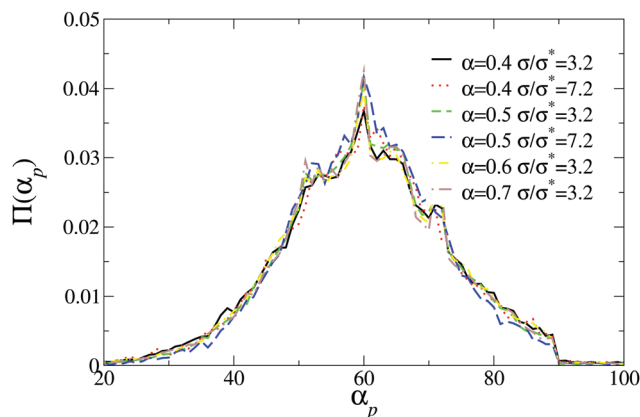


Fig. 13 Average angle distribution for four different asymmetries ($\alpha = 0.4, 0.5, 0.6$ and 0.7) as a function of the grafting density in the gas phase.

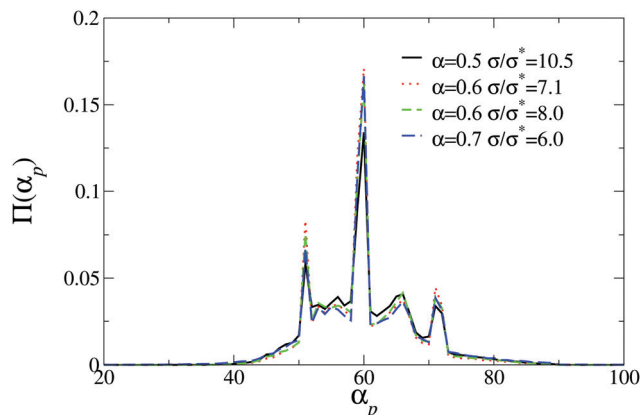


Fig. 14 Average angle distribution for four different asymmetries ($\alpha = 0.4, 0.5, 0.6$ and 0.7) as a function of the grafting density solid phase.

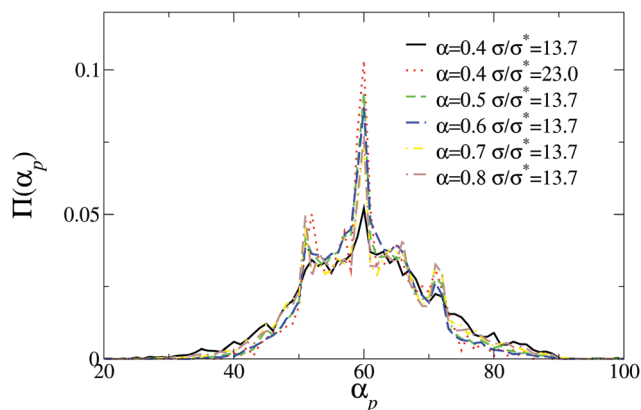


Fig. 15 Average angle distribution for four different asymmetries ($\alpha = 0.4, 0.5, 0.6$ and 0.7) as a function of the grafting density liquid phase.

hence

$$f = \frac{R^3}{\alpha L}. \quad (11)$$

and

$$r_B = \left(\frac{R^3}{\alpha L \sigma} \right)^{1/2}. \quad (12)$$

In order to compare the scaling predictions to the results obtained computationally for R_{corona} , we have to compute the radius of the truncated cone that geometrically defines the pinned micelle (r_b as the smallest base and r_B as the largest one).

Through simple geometrical considerations, we obtain that the radius of a truncated cone of height h at a distance z from the grafting plane is (see Fig. 8):

$$r(z) = r_B + (r_b - r_B) \frac{z}{h}; \quad (13)$$

while the height of the centre of mass of the cone is.

$$z_{\text{cm}} = \frac{h}{4} \frac{r_B^2 + 2r_B r_b + 3r_b^2}{r_B^2 + r_B r_b + r_b^2}, \quad (14)$$

We define R_{corona} as the radius of the truncated cone computed in the centre of mass of the cone: $R_{\text{corona}} = r(z_{\text{cm}})$. We can now use the results obtained for R by solving (9), to obtain a qualitative scaling of the radius of the corona R_{corona} ; we observe that the scaling prediction implies that a shrinkage of R_{corona} with increasing grafting density, as we observe in our numerical simulations (see Fig. 6).

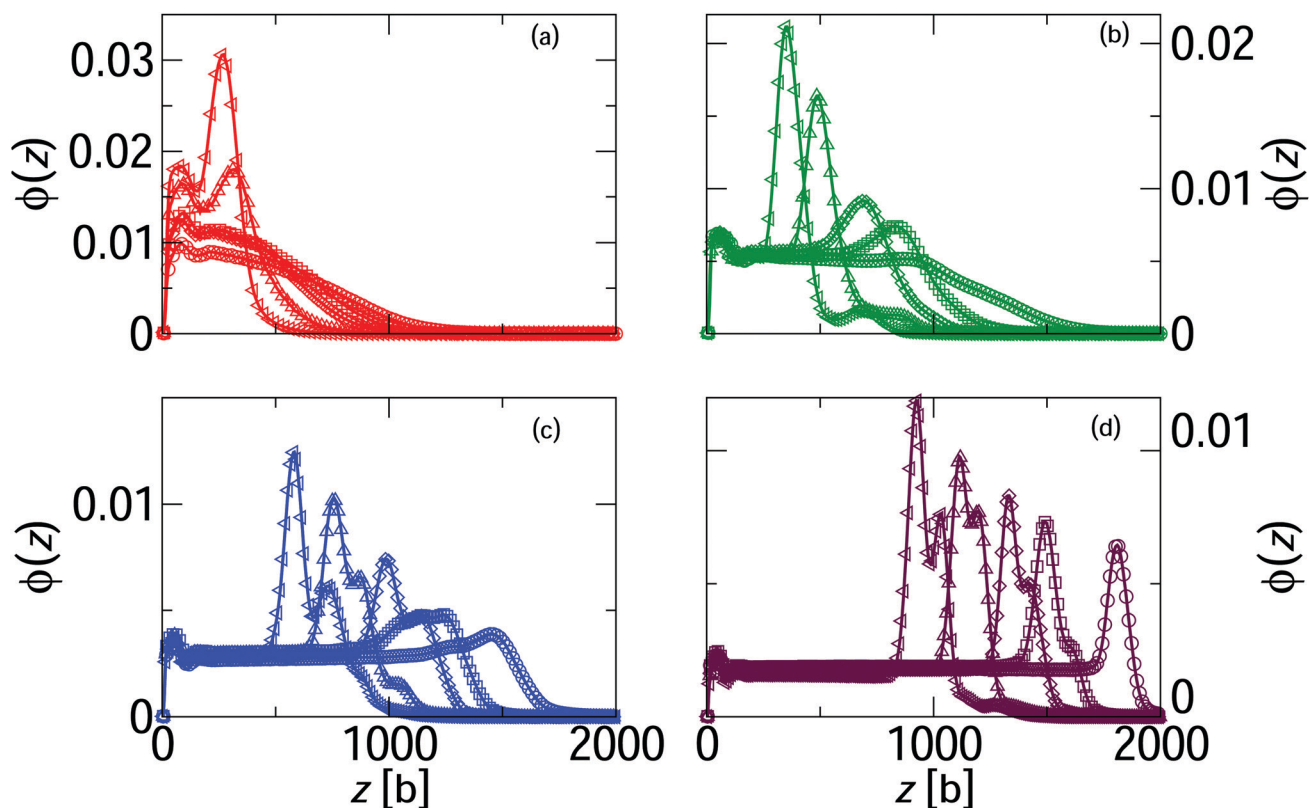


Fig. 16 Height distribution for the brushes with asymmetry ratio $\alpha \in [0.4, 0.8]$ and $\sigma/\sigma^* \in [3.2, 25.8]$. Same colour indicates same grafting density: (a) red for $\sigma = 3.2\sigma^*$; (b) green for $\sigma = 13.7\sigma^*$; (c) blue for $\sigma = 23\sigma^*$; and (d) maroon for $\sigma = 25.8\sigma^*$. Symbols indicate α -values: circles for $\alpha = 0.4$, squares for $\alpha = 0.5$, diamonds for $\alpha = 0.6$, triangles up for $\alpha = 0.7$ and triangles left for $\alpha = 0.8$.

A.2 Cluster analysis

We have carried out a systematic cluster analysis based on the aggregation properties of the solvophobic B-tails, which form the cores of the clusters. Two diblock copolymers are considered to belong to the same cluster if the distance r between the CM's of their B-blocks is less than a chosen cut-off distance r_c ; particles are classified as neighbours if their distance is below r_c and clusters are then built by grouping particles that share at least one neighbour. r_c is a free parameter, that is chosen in a range of values. The determination of the number of patches assembled on the surface is performed as follows. First of all, a patch requires the presence within a cluster (defined in what follows) of at least two different polymers. Second, by making use of our cluster counting algorithm, we analysed the stored configurations obtained during the simulations at various densities, and we identified the groups of solvophobic blobs lying with respect to one another closer than a certain cut-off. The cutoff was empirically identified within a range of values $\Delta r_c \in [100, 200]b$ that discriminates a number $n \neq 1$ of clusters made of more than one chain. Larger values of r_c would inevitably merge all clusters into a single one. In Fig. 13–15, we analyse the orientational distribution between the patches by means of the relative angle α_p formed between the nearest neighbours (Fig. 16).

Acknowledgements

All simulations presented in this paper were carried out on the Vienna Scientific Cluster (VSC). BC acknowledges the Grant of Excellence Departments, MIUR-Italy (ARTICOLO 1, COMMI 314 – 337 LEGGE 232/2016). IC acknowledge support from the Austrian Science Fund (FWF) project 26253-N27. I. C. gratefully acknowledges support from the Ministerio de Economía y Competitividad (MINECO) (FIS2017-89471-R). This work was performed under the Maria de Maeztu Units of Excellence Program from the Spanish State Research Agency Grant No. MDM-2017-0720. This research was supported by Programa Red Guipuzcoana de Ciencia, Tecnología e Información 2019-CIEN-000051-01. We acknowledge support from try BIKAINTEK program (grant no. 008-B1/2020). The authors would like to acknowledge the contribution of the COST Action CA17139.

Notes and references

- 1 S. T. Milner, *Science*, 1991, **251**, 905–914.
- 2 S. Alexander, *J. Phys.*, 1977, **38**, 983–987.
- 3 P. G. de Gennes, *Macromolecules*, 1980, **13**, 1069–1075.
- 4 G. S. Grest, *Macromolecules*, 1994, **27**, 418–426.
- 5 R. R. Netz and M. Schick, *Macromolecules*, 1998, **31**, 5105–5122.
- 6 C. Yeung, K. Huang, D. Jasnow and A. C. Balazs, *Colloids Surf., A*, 1994, **86**, 111–123.
- 7 P. Lai and K. Binder, *J. Chem. Phys.*, 1992, **97**, 586–595.
- 8 P. Lai and K. Binder, *J. Chem. Phys.*, 1991, **95**, 9288–9299.
- 9 I. Coluzza and J.-P. Hansen, *Phys. Rev. Lett.*, 2008, **100**, 016104.
- 10 I. Coluzza, B. Capone and J.-P. Hansen, *Soft Matter*, 2011, **7**, 5255–5259.
- 11 P. Auroy, L. Auvray and L. Léger, *Phys. Rev. Lett.*, 1991, **66**, 719–722.
- 12 A. Halperin, M. Tirrell and T. P. Lodge, *Macromolecules: Synthesis, Order and Advanced Properties*, Springer-Verlag, Berlin/Heidelberg, 1992, vol. 100/1.
- 13 B. Zhao and W. J. Brittain, *Prog. Polym. Sci.*, 2000, **25**, 677–710.
- 14 R. R. Netz and D. Andelman, *Phys. Rep.*, 2003, **380**, 1–95.
- 15 O. Azzaroni, *J. Polym. Sci., Part A: Polym. Chem.*, 2012, **50**, 3225–3258.
- 16 E. B. Zhulina, C. Singh and A. C. Balazs, *Macromolecules*, 1996, **29**, 8254–8259.
- 17 W. Senaratne, L. Andruzzi and C. K. Ober, *Biomacromolecules*, 2005, **6**, 2427–2448.
- 18 R. Barbey, L. Lavanant, D. Paripovic, N. Schüwer, C. Sugnaux, S. Tugulu and H.-A. Klok, *Chem. Rev.*, 2009, **109**, 5437–5527.
- 19 M. Urban, M. A. C. Stuart, W. T. S. Huck, F. Winnik, M. Müller, S. Zauscher, V. V. Tsukruk, G. B. Sukhorukov, I. Luzinov, C. Ober, J. Genzer, I. Szleifer, M. Stamm and S. Minko, *Nat. Mater.*, 2010, **9**, 101–113.
- 20 G. J. Soler-Illia and O. Azzaroni, *Chem. Soc. Rev.*, 2011, **40**, 1107–1150.
- 21 R. Singhvi, A. Kumar, G. P. Lopez, G. N. Stephanopoulos, D. I. Wang, G. M. Whitesides and D. E. Ingber, *Science*, 1994, **264**, 696–698.
- 22 R. M. Choueiri, E. Galati, H. Thérien-Aubin, A. Klinkova, E. M. Larin, A. Querejeta-Fernández, L. Han, H. L. Xin, O. Gang, E. B. Zhulina, M. Rubinstein and E. Kumacheva, *Nature*, 2016, **538**, 79–83.
- 23 E. Zhulina, Y. Lyatskaya and T. Birshtein, *Polymer*, 1992, **33**, 332–342.
- 24 E. B. Zhulina, C. Singh and A. C. Balazs, *Macromolecules*, 1996, **29**, 6338–6348.
- 25 P. G. de Gennes and T. A. Witten, *Phys. Today*, 1980, 51–54.
- 26 B. Capone, I. Coluzza, R. Blaak, F. L. Verso and C. N. Likos, *New J. Phys.*, 2013, **15**, 095002.
- 27 B. Capone, I. Coluzza and J.-P. Hansen, *J. Phys.: Condens. Matter*, 2011, **23**, 194102.
- 28 B. Capone, J.-P. Hansen and I. Coluzza, *Soft Matter*, 2010, **6**, 6075.
- 29 A. Narros, A. J. Moreno and C. N. Likos, *Macromolecules*, 2013, **46**, 3654–3668.
- 30 I. Coluzza, P. D. J. van Oostrum, B. Capone, E. Reimhult and C. Dellago, *Phys. Rev. Lett.*, 2013, **110**, 075501.
- 31 C. Pierleoni, B. Capone and J.-P. Hansen, *J. Chem. Phys.*, 2007, **127**, 171102.
- 32 I. Coluzza, B. Capone and J.-P. Hansen, *Soft Matter*, 2011, **7**, 5255.
- 33 V. Krakoviack, J. P. Hansen and A. A. Louis, *Phys. Rev. E: Stat., Nonlinear, Soft Matter Phys.*, 2003, **67**, 41801.
- 34 A. Narros, C. N. Likos, A. J. Moreno and B. Capone, *Soft Matter*, 2014, **10**, 9601–9614.
- 35 B. Capone, I. Coluzza, F. LoVerso, C. N. Likos and R. Blaak, *Phys. Rev. Lett.*, 2012, **109**, 238301.
- 36 C. I. Addison, J. P. Hansen, V. Krakoviack and A. A. Louis, *Mol. Phys.*, 2005, **103**, 3045–3054.
- 37 B. Capone, C. Pierleoni, J.-P. Hansen and V. Krakoviack, *J. Phys. Chem. B*, 2009, **113**, 3629–3638.

- 38 B. Ladanyi and D. Chandler, *J. Chem. Phys.*, 1975, **62**, 4308–4324.
- 39 N. Metropolis, A. W. Rosenbluth, M. N. Rosenbluth, A. H. Teller and E. Teller, *J. Chem. Phys.*, 1953, **21**, 1087–1092.
- 40 I. Coluzza and D. Frenkel, *ChemPhysChem*, 2005, **6**, 1779–1783.
- 41 N. Osterman, D. Babič, I. Poberaj, J. Dobnikar and P. Ziherl, *Phys. Rev. Lett.*, 2007, **99**, 248301.
- 42 J. Wang and M. Müller, *Macromolecules*, 2009, **42**, 2251–2264.
- 43 E. Zhulina, M. Adam, I. LaRue, S. Sheiko and M. Rubinstein, *Macromolecules*, 2005, **38**, 5330–5351.